applied sciences

MDPI

Article

Fundamental Limits on Spatial Resolution in Ultrafast X-ray Diffraction

Adam Kirrander [1,*] and Peter M. Weber [2]

[1] EaStCHEM, School of Chemistry, University of Edinburgh, David Brewster Road, Edinburgh EH9 3FJ, UK
[2] Department of Chemistry, Brown University, Providence, RI 02912, USA; peter_weber@brown.edu
* Correspondence: Adam.Kirrander@ed.ac.uk; Tel.: +44-(0)131-6504716

Academic Editor: Kiyoshi Ueda
Received: 7 April 2017; Accepted: 17 May 2017; Published: 23 May 2017

Abstract: X-ray Free-Electron Lasers have made it possible to record time-sequences of diffraction images to determine changes in molecular geometry during ultrafast photochemical processes. Using state-of-the-art simulations in three molecules (deuterium, ethylene, and 1,3-cyclohexadiene), we demonstrate that the nature of the nuclear wavepacket initially prepared by the pump laser, and its subsequent dispersion as it propagates along the reaction path, limits the spatial resolution attainable in a structural dynamics experiment. The delocalization of the wavepacket leads to a pronounced damping of the diffraction signal at large values of the momentum transfer vector q, an observation supported by a simple analytical model. This suggests that high-q measurements, beyond 10–15 $Å^{-1}$, provide scant experimental payback, and that it may be advantageous to prioritize the signal-to-noise ratio and the time-resolution of the experiment as determined by parameters such as the repetition-rate, the photon flux, and the pulse durations. We expect these considerations to influence future experimental designs, including source development and detection schemes.

Keywords: X-ray free-electron lasers; ultrafast dynamics; diffraction; spatial resolution; pump-probe; quantum dynamics; wavepackets; photochemistry

1. Introduction

X-ray and electron scattering have long played an important role in structure determination of matter [1–3]. The recent development of ultrashort pulsed electron and X-ray beams has now expanded the scope of structure determination to the time domain [4,5] (and references therein). Important applications include the determination of molecular structures in excited states and the observation of structural molecular dynamics, i.e., the time-resolved determination of transient molecular structures during chemical reactions [6–13]. The advent of ultrafast pulsed X-ray Free-Electron Lasers (XFELs) in particular has increased the intensity of X-rays while decreasing pulse durations to below 30 fs [14]. Consequently, XFELs are assuming a powerful role in the exploration of gas-phase photochemistry, allowing a direct comparison between experimental results and high-level theory [15]. More generally, ultrafast X-ray scattering will play an important and growing role in our arsenal of ultrafast imaging techniques by providing a structurally-sensitive complement to spectroscopic techniques.

Ultrafast measurements typically involve a pump-probe scheme, where a laser pump pulse prepares an initial wavefunction, whose subsequent time evolution is probed at a sequence of delay-times [15–24]. Depending on the experimental situation, the wavepacket may be of electronic [25,26], nuclear [27], or mixed nuclear-electronic [28] nature. Inevitably, the localization of the initially prepared wavepacket and its subsequent spreading depends not only on the potential energy landscape of the molecular system but also on the exact optical preparation of the initially excited state [29–31]. While

in some cases, such as nonradiative transitions in intermediate or statistical limit scenarios, the wave packet is presumed to spread over all receiving modes [32–34]; in other cases, well-defined wave packets persist for at least part of the chemical reaction pathway. In 1,3-cyclohexadiene, for example, the propagation of the wavepacket has been described as 'ballistic', implying that it retains a well-localized form even as it propagates [35]. However, it is inevitable that the nonclassical nature and propagation of the wavepacket leads to a delocalization. It is therefore an important question to consider the extent of this delocalization and how it affects the measurement of the structural dynamics in time-resolved scattering experiments. In the present article, we explore the effective upper limit on the range of the momentum transfer vector (q) that is meaningful to observe in scattering experiments. To do so, we use advanced simulations of ultrafast dynamics in the molecules D_2, ethylene, and 1,3-cyclohexadiene (CHD), and examine the effect of the nuclear wavepacket spreading on the X-ray scattering signals.

2. Methods

2.1. Wavepacket Dynamics

Ultrafast experiments follow the evolution of a time-dependent wavepacket, $|\Psi(\mathbf{r},\mathbf{R},t)\rangle$, where $\mathbf{r}$ and $\mathbf{R}$ are the electronic and nuclear coordinates, and t is time. The wavepacket is the solution to the time-dependent Schrödinger equation,

$$\imath\hbar\frac{d}{dt}|\Psi(\mathbf{r},\mathbf{R},t)\rangle = \hat{H}|\Psi(\mathbf{r},\mathbf{R},t)\rangle, \tag{1}$$

where the Hamiltonian $\hat{H}$ can be decomposed into a field-free molecular Hamiltonian $\hat{H}_0$ and an interaction term $\hat{H}_{\text{int}}$ that describes the interaction with the pump pulse (and, later, the probe pulse). Most commonly, the pump will be an optical laser pulse, so that the light-matter interaction is given in the dipole approximation by $\hat{H}_{\text{int}}(t) \approx -d\epsilon(t)$, where $\epsilon(t)$ is the time-dependent electromagnetic field and d the electric dipole operator. The wavepacket excited by the pump pulse will have certain qualitites imprinted by the pump laser, including a bandwidth, phase-properties, and overall energy distribution.

There are many strategies for solving the time-dependent Schrödinger equation in Equation (1) above. One possible ansatz expands the wavepacket in the complete basis of orthonormal eigenstates $|\Psi_j\rangle$ of the molecular Hamiltonian $\hat{H}_0$ (see e.g., Ref. [36]),

$$|\Psi(t)\rangle = \sum_j c_j(t)e^{-iE_jt/\hbar}|\Psi_j\rangle, \tag{2}$$

where $|\Psi(t)\rangle$ is the excited wavepacket, $|\Psi_j\rangle$ are orthonormal rovibronic wave functions and E_j are the corresponding energies. According to first-order perturbation theory, the time-dependent coefficients $c_j(t)$ become,

$$c_j(t) = iD_{js}\left[\frac{e}{\hbar}\int_{-\infty}^{t} dt e^{i\omega_{js}t}\epsilon(t')\right], \tag{3}$$

where D_{js} are the combined dipole transition moments and the Franck–Condon factors for excitation from the initial state s to the final state j. The expression in the square brackets corresponds to the energy- and the time-dependent complex excitation function with e the charge of an electron, the angular frequency $\omega_{js} = (E_j - E_s)/\hbar$ and $\epsilon(t')$ the excitation field [28,37,38]. The trouble with this solution is that it requires that the eigenstates of the system are calculated first, which renders the approach practical only in molecules with a small number of degrees of freedom, such as the diatomic molecule D_2 in the present article.

In the general case, one must propagate the wavepacket numerically while circumventing as much as possible the effect of the exponential scaling of the required grid (basis) with the number of degrees of freedom. One approach is to expand the molecular wavepacket in a basis of non-stationary Gaussian wavefunctions (coherent states). Methods that take this path include the

ab-initio multiconfigurational Ehrenfest method (AI-MCE) [39,40] used in this article, the closely related ab-initio multiple spawning (AIMS) [41], the hybrid ab-initio multiple cloning (AIMC) method [42], the variational multiconfigurational Gaussians (v-MCG) [43] method, and the coupled coherent-states (CCS) method [44–46]. All of these methods trace their roots to seminal semi-classical work by Eric Heller [47].

In AI-MCE, the molecular wavepacket, $|\Psi(t)\rangle$, is expanded in terms of Ehrenfest functions with dynamically coupled expansion coefficients $D_k(t)$,

$$|\Psi(t)\rangle = \sum_{k=1}^{N} D_k(t)|\psi_k(t)\rangle, \tag{4}$$

where each Ehrenfest function, $|\psi_k(t)\rangle$, consists of a Gaussian nuclear coherent state, $|\bar{\mathbf{z}}_k(t)\rangle$, distributed across N_s electronic states, $|\phi_k^i\rangle$, with the amplitudes $a_k^i(t)$,

$$|\psi_k(t)\rangle = \left[\sum_{i=1}^{N_s} a_k^i(t)|\phi_k^i\rangle\right] |\bar{\mathbf{z}}_k(t)\rangle. \tag{5}$$

The coherent state, $|\bar{\mathbf{z}}_k(t)\rangle$, is a product of 3×(number of atoms) one-dimensional Gaussian coherent states, shown here for x_α, the x-component of the coordinate of atom α,

$$\langle x_\alpha|\bar{\mathbf{z}}_k(t)\rangle = \left(\frac{\gamma_\alpha}{\pi}\right)^{\frac{1}{4}} \exp\left(-\frac{\gamma_\alpha}{2}\left(x_\alpha - Q_{\alpha x}^k\right)^2 + \frac{\imath}{\hbar}P_{\alpha x}^k\left(x_\alpha - Q_{\alpha x}^k\right) + \frac{\imath P_{\alpha x}^k Q_{\alpha x}^k}{2\hbar}\right), \tag{6}$$

where the position is $Q_{\alpha x}^k$, the momentum $P_{\alpha x}^k$, and the width parameter γ_α. The Ehrenfest ansatz can be slow to converge, but, in the context of this article, the difference is mostly technical, as sampling methods have been developed to speed up the convergence of Equation (4) [42,48]. Each time-step of the propagation requires multiple calls to an ab-initio electronic structure software package to calculate energies for the ground and excited states, the potential gradients, and non-adiabatic couplings. For further details, see, e.g., Refs. [39,40,42,49]. In this article, we use the AI-MCE method to simulate the photoexcited dynamics of the molecules ethylene and CHD.

2.2. Computational Details for Dynamics

2.2.1. Deuterium (D_2)

In D_2, we consider a vibrational wavepacket in the $B^1\Sigma_u^+$ electronic state, excited by a single photon from the $X^1\Sigma_g^+(v=0)$ ground state. The pump pulse energy is 14.3 eV, with the full width at half maximum (FWHM) duration 20 fs, such that the excited vibrational wavepacket is centered at the $v = 38$ vibrational state [27]. The potential energy curves are shown in Figure 1a. Since D_2 is a diatomic molecule, the wavepacket can be expanded in a basis of vibrational eigenfunctions using the ansatz in Equation (2). We use potential energy curves for the initial ground X-state [50] and the excited B-state [51], and dipole transition moments [52], calculated ab-initio by Wolniewicz et al. The molecular mass is taken from CODATA 2010 [53]. The vibrational eigenfunctions are calculated using an accurate 5th order Runge–Kutte algorithm, with the orthonormality of the vibrational eigenstates ensured via a Cholesky factorisation, and the transition moments D_{js} calculated for $B^1\Sigma_u^+(v) \leftarrow X^1\Sigma_g^+(v=0)$.

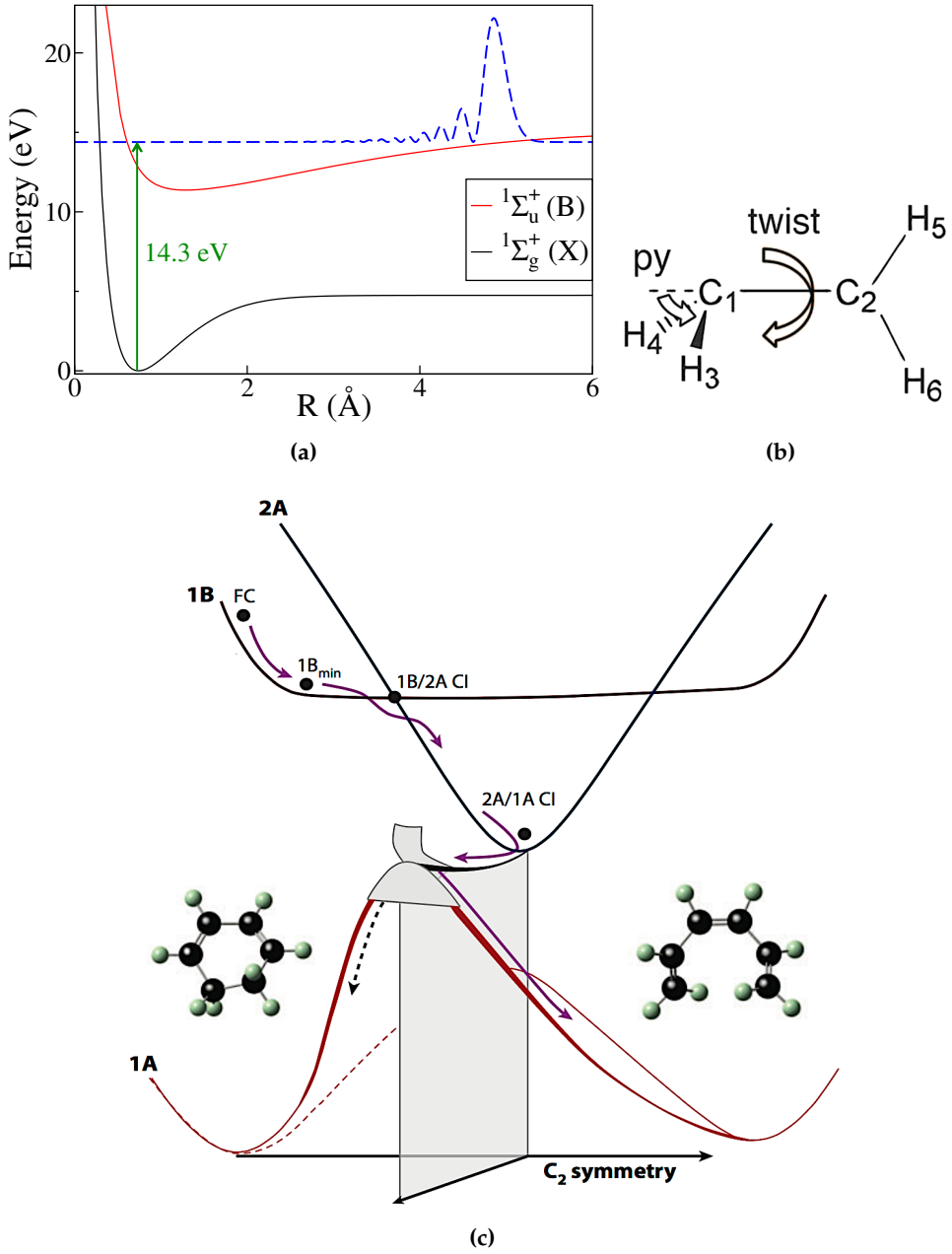

Figure 1. Overview of the molecules and dynamics discussed in this article. (**a**) D_2: Potential energy curves for the ground $X^1\Sigma_g^+$ and excited $B^1\Sigma_u^+$ state potential energy curves. The vibrational wavepacket is excited onto the $B^1\Sigma_u^+$ state centered on vibrational state $v = 38$ by a 14.3 eV pump pulse. The wavepacket (dashed line) is shown at the outer turning point; (**b**) Ethylene: After excitation to the S_1 state, the dynamics is dominated by C–C bond twist, pyramidalization, and changes in C–C bond length; (**c**) 1,3-cyclohexadiene (CHD): Upon excitation from the 1A ground state onto the 1B bright state in the Franck–Condon region, the molecule decays through a sequence of conical intersections back to the ground state in either the ring-open or ring-closed form (based on illustration in Ref. [54]).

2.2.2. Ethylene

In ethylene ($H_2C{=}CH_2$), we consider vertical excitation into the S_1 ($\pi\pi^*$) state. The excited molecule undergoes cis-trans isomerisation around the C=C bond, and decays via nonradiative decay through a twisted or pyramidalised conical intersection, or via H-atom migration to form ethylidene (CH_3CH), which then decays through a different conical intersection. The basic dynamics is sketched

out in Figure 1b. The population on S_1 remains fairly constant for the first 30 fs, at which point the molecule begins to decay exponentially to S_0 with an approximate lifetime of ≈112 fs.

The simulations employ the AI-MCE method [55], with electronic potential energies, gradients, and nonadiabatic couplings calculated *on-the-fly* using the MOLPRO electronic structure package [56]. A total of 1000 Ehrenfest trajectories are initiated in the Franck–Condon region using a Wigner distribution [57], and are propagated for 150 fs. The electronic structure is calculated at the state-averaged SA3-CAS(2,2)-SCF/cc-pVDZ level (two electrons in π and π^* orbitals) including the S_0, the S_1 π-π^*, and the S_2 π^{*2} states. The calculated lifetime from the simulations (112 fs) agrees well with the 110 fs obtained with AIMS dynamics using the same CAS(2,2) active space [58]. Including more dynamic correlation via CASPT2 drops the lifetime to 89 fs [58] while including Rydberg states (predominantly the π-3s state) lowers the lifetime further to approximately 60 fs [59,60]. However, the influence of Rydberg states on the dynamics simulations is relatively small and experimental evidence for the role of Rydberg states remains under debate [61,62]. Importantly, the small active space in the present study allows us to converge the simulations [49], which is the key aspect for the present discussion of X-ray scattering signals.

2.2.3. 1,3-Cyclohexadiene (CHD)

The electrocyclic ring-opening reaction of CHD has been studied extensively in experiments [54], including ultrafast X-ray scattering [6] and time-resolved photoelectron spectroscopy [15]. Following vertical excitation into the 1B bright state, the molecule decays rapidly via two sets of conical intersections back to the 1A ground state, as outlined in Figure 1c. The reaction is very rapid and occurs in a ballistic manner. When the molecule reaches the ground state, there is an approximately even split between molecules that return to the ring-closed form and those that undergo ring-opening [6,54].

The simulations follow the procedure outlined in Ref. [6]. The same AI-MCE method as in the ethylene case is used, with adiabatic electronic potential energies, gradients, and nonadiabatic couplings calculated *on-the-fly* with MOLPRO [56] at the SA3-CAS(6,4)-SCF/cc-pVDZ level of theory, which has been shown to be suitable for the CHD ring-opening reaction [63]. Wigner-sampling is employed for the initial state, with 100 AI-MCE trajectories propagated for 200 fs. This is not sufficient to fully converge the simulations, but provides a reasonable and effectively semi-classical representation of the reaction dynamics.

2.3. X-ray Scattering

We now review briefly the theory of X-ray scattering. To a good approximation, X-ray photons scatter in a two-photon process via the squared field vector potential, A^2, taken in the first order of perturbation theory (see e.g., Refs. [64,65]). The resulting double-differential scattering cross-section is given by [66,67],

$$\frac{d^2S}{d\Omega d\omega_{k_1}} = \alpha \int_0^\infty dt \int_{-\infty}^\infty d\delta \, I_P(t) C_P(\delta) e^{-\imath \omega_{k_1} \delta} \mathcal{W}(t,\delta), \tag{7}$$

where $I_P(t) = |E_{k_0}|^2 e^{-(t-t_P)^2/\gamma_d^2}$ is the X-ray pulse intensity-profile, and $C_P(\delta) = \sqrt{\epsilon(\delta)} e^{\imath \omega_{k_0} \delta}$ the normalized X-ray pulse coherence function. The probe pulse duration, in terms of FWHM intensity, is $\tau_d = 2\gamma_d \sqrt{\ln 2}$, and $\epsilon(\delta) = e^{-(t-t_P)^2/2\gamma_d^2}$ is the Gaussian electric field envelope, with t_P the time-delay between pump and probe. The scattering from the material system is given by $\mathcal{W}(t,\delta)$, which is a function of the wavepacket $|\Psi(t)\rangle$ and the scattering operator $\hat{L}$,

$$\mathcal{W}(t,\delta) = \langle \Psi(t) | e^{\imath \hat{H}_0 \delta/2\hbar} \, \hat{L}^\dagger \, e^{-\imath \hat{H}_0 \delta/\hbar} \, \hat{L} \, e^{\imath \hat{H}_0 \delta/2\hbar} | \Psi(t) \rangle, \tag{8}$$

where the scattering operator $\hat{L}$ appears twice as appropriate for a two-photon process, and is given by

$$\hat{L} = \sum_j e^{\imath \mathbf{q} \mathbf{r}_j}, \tag{9}$$

where $\mathbf{r}_j$ is the position of electron j, and $\mathbf{q} = \mathbf{k}_0 - \mathbf{k}_1$ the momentum transfer vector with $\mathbf{k}_0$ and $\mathbf{k}_1$ the incoming and outgoing wavevectors for the X-rays. Matrix elements of the operator $\hat{L}$ correspond to elastic and inelastic scattering [68]. Assuming that the time-scale for nuclear motion is significantly slower than for electrons, and that electronic states are well separated, one arrives at the so-called elastic approximation [67,69],

$$\mathcal{W}(t,\delta) \propto \sum_i \int |\chi_i(\mathbf{R},t)|^2 \, |L_{ii}|^2 \; d\mathbf{R}, \tag{10}$$

in which we have used the Born–Huang ansatz for the wavepacket $|\Psi(\mathbf{R},t)\rangle = \sum_i \chi_i(\mathbf{R},t)|i(\mathbf{r};\mathbf{R})\rangle$, with $\chi_i(\mathbf{R},t)$ the nuclear wavepacket on each electronic state $|i(\mathbf{r};\mathbf{R})\rangle$, and the elastic X-ray scattering matrix elements $L_{ii} = \langle i(\mathbf{r};\mathbf{R})|\hat{L}|i(\mathbf{r};\mathbf{R})\rangle_{\mathbf{r}}$ [70–72]. The elastic scattering can be simplified further if we adopt the independent atom model (IAM), whereby we ignore the specifics of each electronic state and instead assume that the bulk of the scattering corresponds to a coherent sum of the scattering from the individual constituent atoms. In this approximation, $L_{ii} \approx f_{\mathrm{IAM}}$, irrespective of electronic state i. The f_{IAM} is given by,

$$f_{\mathrm{IAM}}(\mathbf{q}) = \sum_{\alpha=1}^{N_{at}} f_\alpha^0(q) e^{i\mathbf{R}_\alpha \mathbf{q}}, \tag{11}$$

where $f_\alpha^0(q)$ are the tabulated atomic form factors [73], $\mathbf{R}_\alpha$ the atomic positions, and $q{=}|\mathbf{q}|$ the amplitude of the momentum transfer, which is a function of the scattering angle θ via $q = 2|\mathbf{k}_0| \sin\theta/2$. Finally, $|L_{ii}|^2 \approx |f_{\mathrm{IAM}}|^2$ becomes,

$$|f_{\mathrm{IAM}}(\mathbf{q})|^2 = \sum_{\alpha=1}^{N_{at}} \left|f_\alpha^0(q)\right|^2 + \sum_{\alpha\neq\beta}^{N_{at}} f_\alpha^0(q) f_\beta^0(q) e^{i\mathbf{R}_{\alpha\beta}\mathbf{q}}, \tag{12}$$

with $\mathbf{R}_{\alpha\beta} = \mathbf{R}_\alpha - \mathbf{R}_\beta$ the vector between each pair of atoms. The first sum on the right is the atomic term, which forms a constant background, and the second sum is the molecular term, which contains all structural interference relating to molecular geometry. Equation (12), when rotationally averaged, becomes the standard IAM formula shown in Equation (15). It is perhaps worthwhile to point out that elastic electron scattering results in an expression almost identical to Equation (12), with the main difference being that the form factors for electron scattering must account for the additional scattering from the nuclei [2,74,75].

3. Results

3.1. Simple Model

We begin by examining the effect of the delocalization of the nuclear wavepacket on the diffraction signal via a simple analytical model. For this, we use frozen Gaussian width parameters, γ_α, fitted to calculated ground state harmonic vibrational wavefunctions in a large set of organic molecules by Thompson et al. [76]. Consider a Gaussian nuclear wavepacket, $v(\mathbf{R})$, expressed as a product of three-dimensional Gaussian wavefunctions, one for each atom. The probability density for such a wavepacket is,

$$|v(\mathbf{R}_1,\ldots,\mathbf{R}_{N_{\mathrm{at}}})|^2 = \prod_{\alpha=1}^{N_{\mathrm{at}}} \left(\frac{\gamma_\alpha}{\pi}\right)^{\frac{3}{2}} e^{-\gamma_\alpha(\mathbf{R}_\alpha - \mathbf{Q}_\alpha)^2}, \tag{13}$$

where $\mathbf{R}_\alpha = (R_{\alpha x}, R_{\alpha y}, R_{\alpha z})$ are the Cartesian nuclear coordinates, $\mathbf{Q}_\alpha$ is the coordinate that determines the center of the wavepacket, N_{at} is the number of atoms, and γ_α the width parameter of the Gaussian associated with each atom. There is a large body of theoretical work that shows that such Gaussian wavepackets constitute a sensible basis for nuclear dynamics (see e.g., Refs. [40,43,44,47,77]). Time-dependent propagation of the wavepacket generally involves propagation

(classical, semi-classical, or quantum) of the phase-space coordinates and sometimes the width parameter γ_α.

The X-ray scattering signal will be proportional to $\langle v(\mathbf{R})| \left|f_{\mathrm{IAM}}(q)\right|^2 |v(\mathbf{R})\rangle_{\mathbf{R}}$, according to the elastic approximation in Equation (10). Solving this integral analytically, including rotational averaging and thus assuming no preferred orientation of the molecule, results in,

$$I_{\mathrm{IAM}}^{\mathrm{wavepacket}}(q) \propto \sum_{\alpha=1}^{N_{\mathrm{at}}} \left|f_\alpha^0(q)\right|^2 + \sum_{\beta\neq\alpha}^{N_{\mathrm{at}}} f_\alpha^0(q) f_\beta^0(q) \frac{\sin\left(qQ_{\alpha\beta}\right)}{qQ_{\alpha\beta}} e^{-q^2/2\gamma_{\alpha\beta}}, \tag{14}$$

with $Q_{\alpha\beta} = \left|\mathbf{Q}_\alpha - \mathbf{Q}_\beta\right|$ the distance between centers of the Gaussian wavepackets for each pair of atoms, and with the damping factor $\exp\left(-q^2/2\gamma_{\alpha\beta}\right)$ proportional to the combined Gaussian width of the two atoms given by $\gamma_{\alpha\beta} = 2\gamma_\alpha\gamma_\beta/\left(\gamma_\alpha + \gamma_\beta\right)$. The consequence of introducing the wavepacket in Equation (13) is thus an exponential damping of the molecular term in the scattering, which leaves the atomic term unaffected. It is instructive to contrast Equation (14) with the standard rotationally averaged IAM expression for scattering, originally derived by Debye [78],

$$I_{\mathrm{IAM}}(q) \propto \sum_{\alpha=1}^{N_{\mathrm{at}}} \left|f_\alpha^0(q)\right|^2 + \sum_{\beta\neq\alpha}^{N_{\mathrm{at}}} f_\alpha^0(q) f_\beta^0(q) \frac{\sin\left(qR_{\alpha\beta}\right)}{qR_{\alpha\beta}}, \tag{15}$$

where $R_{\alpha\beta}$ are the distances between atoms (i.e., $\mathbf{R}_\alpha$ are the fixed nuclear positions). This expression is recovered from the wavepacket-damped expression in Equation (14) for strong localization ($\gamma_\alpha \to \infty$). Conversely, strong *de*localization ($\gamma_\alpha \to 0$) extinguishes the structural interference in the molecular term, which is responsible for structural information. It is interesting to note that the damping in Equation (14) takes the same form as the temperature damping derived in electron diffraction [2], but has nothing to do with temperature; it is a consequence of the inherently delocalized nature of the wavepacket [21].

Numerically, we can examine the damping factor $\exp -q^2/2\gamma_{\alpha\beta}$ using the Gaussian widths determined by Thompson et al. [76]. The results, calculated in the range $0 < q < 20$ Å^{-1} are shown in Figure 2 for pairs of atoms. For each pair, the damping factor is calculated for $\gamma_\alpha \pm \sigma_\alpha$, where σ_α is the standard deviation obtained in the fitting procedure for the width parameters γ_α in Ref. [76]. Numerical values for the damping factors at $q = 10$ Å^{-1} are shown in Table 1. Invariably, the damping at $q = 10$ Å^{-1} is on the order of 0.7 or less (down to ≈0.4 for H, but then H-atoms contribute little to the scattering signal [75]). A factor of 0.7 corresponds to 30% of the signal irrevocably lost due to the delocalized nature of the target. It is important to point out that these damping factors constitute *lower* limits, since the width parameters used here are essentially minimum width parameters fitted to ground state harmonic oscillators. As such they are representative of the initially pumped wavepacket in the Franck–Condon region above the ground state geometry. It is therefore clear that, generally, we can expect significant degradation of the diffraction signal for $q > 10$ Å^{-1}. The subsequent evolution of the wavepacket then leads to further dispersion, and we will investigate the effects of the propagation of the wavepacket for the three molecules D_2, ethylene, and CHD, in Section 3.2.

Table 1. The damping factor (see Equation (14)) at $q = 10$ Å^{-1} for pairs of atoms, including: H, C, N, O, F, S, and Cl. A damping factor with value 1 corresponds to no damping (100% of the signal remains), and 0 to complete damping (the signal vanishes). In parenthesis, the value of the damping factor for $\gamma_\alpha - \sigma_\alpha$, with σ_α the standard deviation, is given to provide an approximate lower bound. The numerical values for γ_α and σ_α are taken from Ref. [76].

Atom	H	C	N	O	F	S	Cl
H	0.22 (0.17)	0.40 (0.33)	0.39 (0.31)	0.35 (0.27)	0.31 (0.21)	0.38 (0.28)	0.29 (0.17)
C		0.73 (0.65)	0.71 (0.61)	0.64 (0.54)	0.57 (0.40)	0.69 (0.54)	0.53 (0.33)
N			0.69 (0.58)	0.62 (0.50)	0.55 (0.38)	0.67 (0.51)	0.52 (0.32)
O				0.56 (0.44)	0.50 (0.33)	0.61 (0.45)	0.47 (0.28)
F					0.44 (0.25)	0.54 (0.34)	0.41 (0.21)
S						0.66 (0.45)	0.50 (0.28)
Cl							0.39 (0.17)

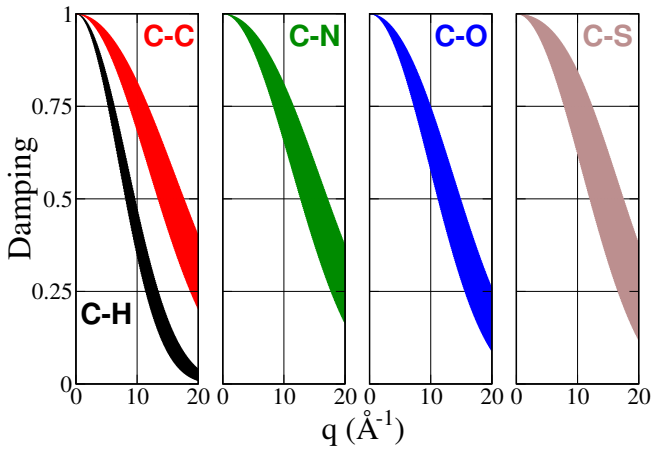

Figure 2. Damping factors (see Equation (14)) as a function of momentum transfer q (Å^{-1}) calculated using frozen Gaussian widths γ_α from Thompson et al. [76] for scattering from the following pairs of atoms: C−H, C−C, C−N, C−O, and C−S. The damping is given for $\gamma_\alpha \pm \sigma_\alpha$, where σ_α are the standard deviations in the fitted widths [76].

3.2. Simulations

Having considered a simple analytic model of the effect of delocalization on the diffraction pattern in the previous section, we now turn to simulations to examine the effect of the propagation of the molecular wavefunction on the scattering signal. We consider three different molecules to emphasize the generality of the discussed effects. In D_2 (Section 3.2.1), we examine the effect in a prototypical diatomic molecule, compare the results to a classical molecule, and evaluate the effect of nuclear mass on the wavepacket and thus the scattering signal. In ethylene (Section 3.2.2), we use the fact that quantum molecular dynamics simulations can be fully converged in such a comparatively small molecule to examine the sensitivity of the scattering signal to the number of trajectories used as a nuclear basis in the simulations. Finally, in CHD (Section 3.2.3), we examine the case of a larger polyatomic molecule, and in particular, evaluate the effect of the width parameters associated with the nuclear basis.

3.2.1. Deuterium (D_2)

We begin by considering the vibrational wavepacket in the B-state of the diatomic molecule D_2. The probability distribution of the wavepacket is shown in a contour plot in Figure 3a as a function of time and internuclear distance R. Upon excitation at the inner turning point by the 20 fs pump pulse, the wavepacket oscillates between the inner and outer turning points of the B-state potential with

a period of 82 fs. Due to the anharmonic nature of the potential, the wavepacket gradually spreads across the entire B-state potential. It is worth emphasizing that this wavepacket has been observed in a recent experiment using a strong-field probe [27].

The elastic X-ray scattering corresponding to this wavepacket is shown in Figure 3b as a function of time and momentum transfer q. In order to focus on the structural component of the diffraction, and to remove the atom-specific effects of the form factors, we plot the *modified molecular intensity* [74],

$$M(q,t) = qI_{\mathrm{mol}}(q,t) / \left|f_m^0(q)\right| \left|f_n^0(q)\right|, \tag{16}$$

with $f_m^0 = f_n^0 = f_{\mathrm{H}}^0$ in the present case. The molecular intensity, $I_{\mathrm{mol}}(q,t)$, is calculated as $I_{\mathrm{mol}}(q,t) = \langle\Psi(t)|\sum_{i\neq j} f_i^0(q) f_j^0(q) \sin qR_{ij}/qR_{ij}|\Psi(t)\rangle$, which thus combines the elastic scattering approximation in Equation (10) and the IAM in Equation (12). The modified molecular intensity makes it easier to visualize the elastic scattering intensity at larger values of q, which otherwise decays rapidly due to the exponential decay of the atomic form factors $f^0(q)$ [74]. We assume an instant X-ray probe pulse, $\delta(t - t_P)$, to avoid convolution over the temporal X-ray pulse envelope, which would otherwise act to further '*soften*' the diffraction patterns and thus obscure the effect of the wavepacket on the scattering.

Since D_2 has a small reduced mass the wavepacket is strongly delocalized from the beginning, even when excited by a bandwidth limited pulse as in the present example. The resulting diffraction signal is thus strongly damped from the outset, as can be seen at high q values in Figure 3b. It is enlightening to compare the diffraction pattern in Figure 3b to that of a classical D_2 molecule, shown in Figure 3c, in which the nuclei are perfectly localized at all times. The diffraction from the classical molecule is shown for three full oscillations, at the same frequency as the quantum D_2 wavepacket ($T = 82$ fs). Comparing the diffraction patterns from the classical and quantum D_2 molecule, it is apparent that the signal in the classical case is stronger and better defined across all values of q, and remains identical for each oscillation. In contrast, the quantum wavepacket disperses with time, see $t/T > 5$ in Figure 3a, an effect which increases the decay of the diffraction signal over time, as seen in Figure 3b.

One possible objection to using D_2 as an example, despite the fact that the modified molecular intensity minimizes the effect of the atomic form factors on the scattering, is that D_2 is not an obvious candidate for a scattering experiment and that its small reduced mass exaggerates delocalization. We have therefore performed the same calculation but with a higher reduced mass corresponding to the potassium dimer, K_2. In order to aid comparison, we have not changed the potential, i.e., the potential energy curve remains that of the D_2 B-state, and all parameters except the reduced mass are left unchanged. We refer to this wavepacket as $\tilde{K}_2$ to avoid confusion with actual K_2. We first consider the wavepacket, which is plotted in Figure 4a. The greater reduced mass leads to a significant increase in the density of vibrational states, and thus in the number of eigenstates contained in the wavepacket in Equation (2). As a consequence, initial localization is stronger than in D_2, but conversely, the dispersion at longer times (on the normalized t/T timescale) is also greater. The scattering from the $\tilde{K}_2$ wavepacket, shown in Figure 4b, is thus more defined at earlier time, but suffers more from the dispersion of the wavepacket at larger multiples of the characteristic period, which leads to a more marked degradation of the diffraction signal at large values of q.

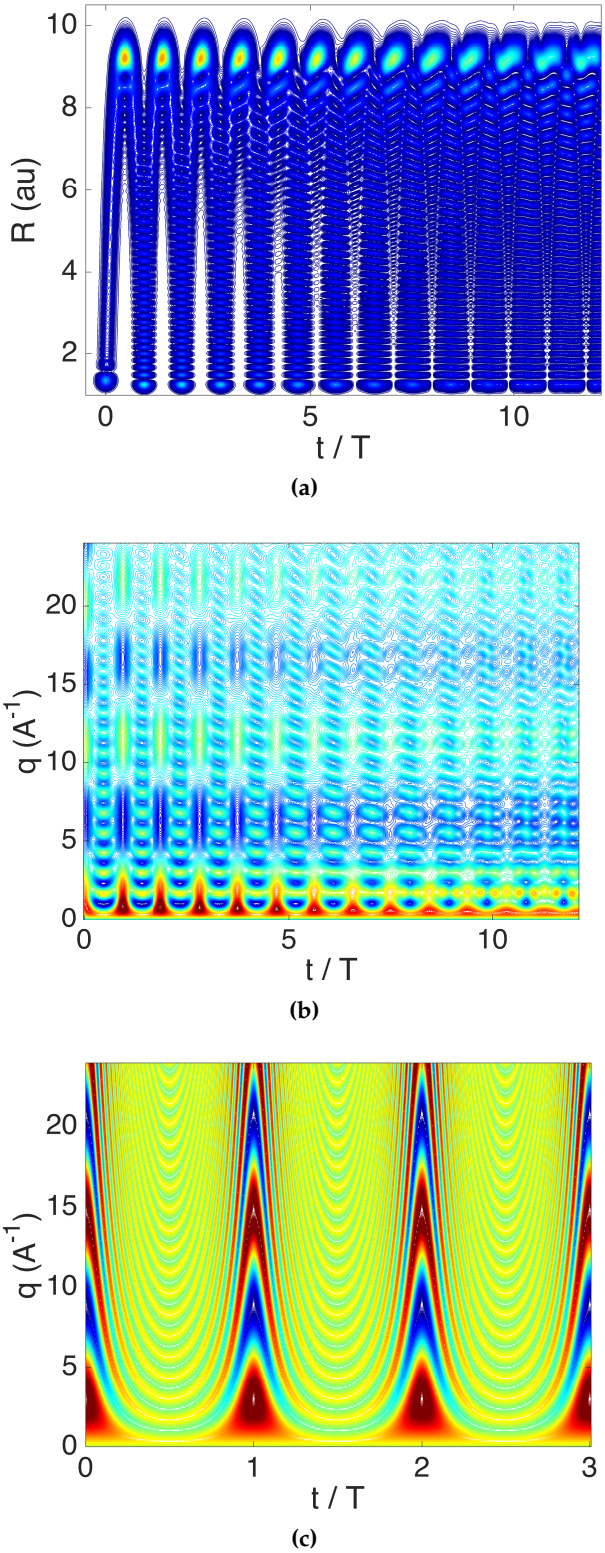

Figure 3. Results for D_2 excited to the electronic B-state by a 14.3 eV pulse with 20 fs duration. (**a**) Contour plot of the D_2 vibrational wavepacket probability density, $|v(R,t)|^2$, with R the internuclear distance in Bohr and t the time; (**b**) Contour plot of the corresponding modified (elastic) scattering intensity $M(q,t)$ for the wavepacket, with q the momentum transfer in Å^{-1} and t the time; (**c**) Contour plot of the modified (elastic) scattering intensity $M(q,t)$ for the *classical* D_2 molecule, shown over three oscillation periods, $t \in [0, 3T]$. Note that in all three plots the time t is given in units of the classic oscillation period $T = 82.5$ fs. The modified scattering intensity $M(q,t)$ is defined in Equation (16), and we use the form factor for H in the denominator.

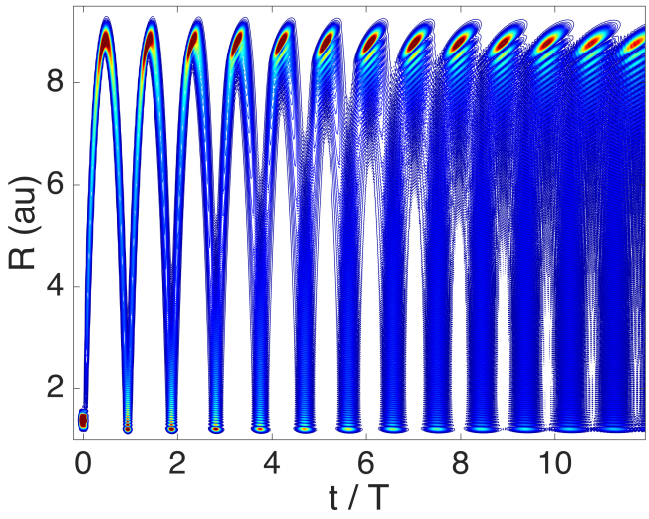

(a)

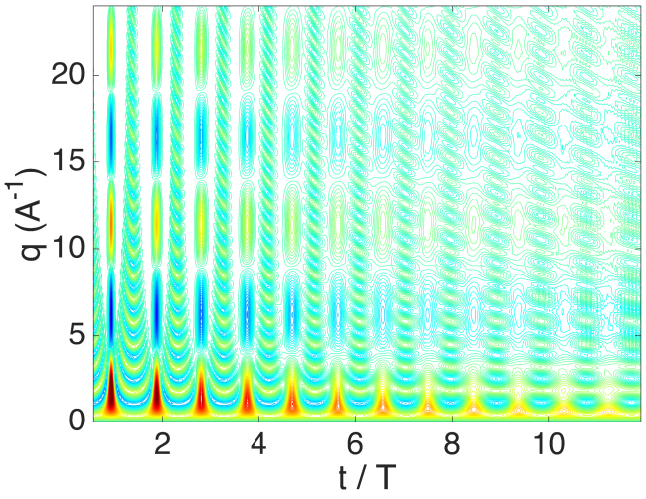

(b)

Figure 4. Results for $\tilde{K}_2$, calculated using the reduced mass of K_2 and the B-state potential of D_2, excited to the electronic B-state by a 14.3 eV pulse with 20 fs duration. (**a**) The $\tilde{K}_2$ vibrational wavepacket probability density, $|v(R,t)|^2$, with R the internuclear distance in Bohr and t the time; (**b**) Contour plot of the corresponding modified (elastic) scattering intensity, $M(q,t)$, with q the momentum transfer in Å^{-1} and t the time. In both plots, the time t is given in units of the classic oscillation period $T = 335.8$ fs. The modified scattering intensity $M(q,t)$ is defined in Equation (16), and we use the form factor for K in the denominator.

3.2.2. Ethylene

We now consider ethylene, a small molecule where we can be confident that the simulations are converged, to investigate the effect of the number of trajectories included in the simulations. In the case of ethylene, full convergence requires >500 trajectories [49]. In Figure 5, we compare the modified molecular intensity for elastic scattering from ethylene for a small set of 20 trajectories, shown in Figure 5a, with a large set of 1000 trajectories shown in Figure 5b. Comparison of the two signals indicates that the subset of 20 trajectories underestimates the dispersion at longer times, with the full set of 1000 trajectories showing a distinct deterioration of the signal over time. Interestingly, the limited subset of 20 trajectories *is* sufficient to capture the evolution of the dynamics qualitatively. In part, this reflects that the diffraction signal is dominated by the comparatively simple dynamics of the

C–C bond [75], which is well reproduced by the smaller subset of trajectories, but the observation is more general since we know from earlier studies that a small number of trajectories can do a good job of capturing the essence of a reaction path [79]. This observation is also commensurate with recent work on the ring-opening reaction of CHD, which found that the time-dependent diffraction pattern for the reaction could be reproduced accurately by a comparatively small number of trajectories representative of the dynamics [6]. Overall, this is good news for the analysis of ultrafast diffraction experiments because it suggests that a sensible analysis of experimental results does not require fully converged quantum molecular dynamics simulations (which are simply out of reach in many molecules of interest). However, it does raise another issue, which is the influence of the width parameters associated with trajectories, as discussed in the example of CHD next.

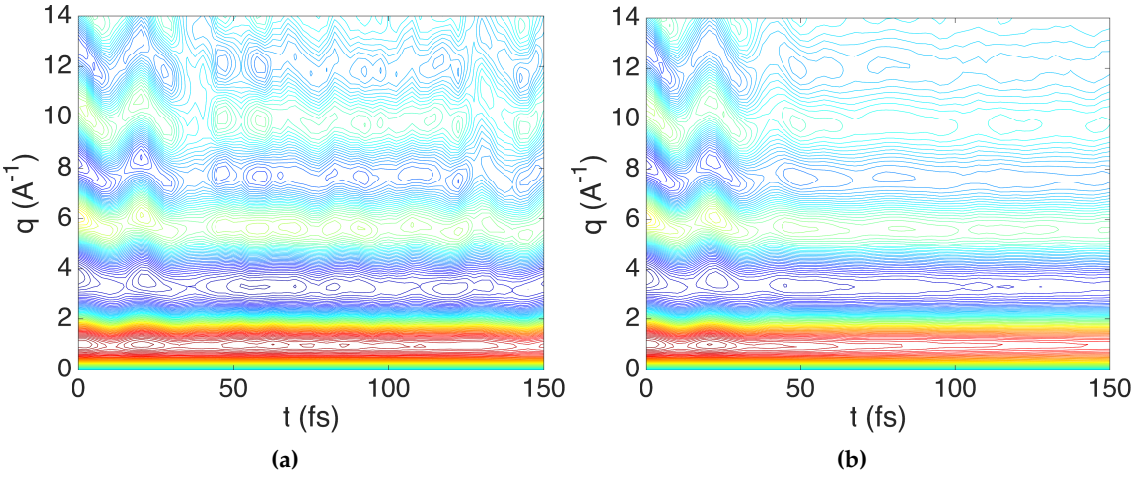

Figure 5. Contour plots of modified (elastic) scattering intensity, $M(q,t)$, for the photoexcited dynamics of ethylene. Time in fs and momentum transfer q in Å^{-1}, with $M(q,t)$ defined in Equation (16) (we use form factors for the C-atom in the denominator). (**a**) A small set of 20 trajectories; (**b**) A large set of 1000 trajectories, giving a better representation of dispersion of the wavepacket at long times.

3.2.3. 1,3-Cyclohexadiene (CHD)

We consider the elastic scattering from the polyatomic molecule CHD during the electrocyclic ring-opening reaction triggered by an optical pump pulse [6,15], as outlined in Section 2.2.3. A reduced-dimensionality representation of the dominant dynamics is shown in Figure 6, in terms of the length of the C–C bond that breaks during the ring-opening reaction. Here, we will focus on the effect of the wavepacket width parameters γ_α defined in Equation (6) on the diffraction signal. We show the scattering in terms of the modified molecular intensity, Equation (16), with $f_m^0 = f_n^0 = f_C^0$. Note that the simulations are identical in all three scenarios discussed below, and only the γ_α parameters are varied. Note that fully converged simulations with an oversampled nuclear basis would not display a dependence on γ_α in the scattering.

First, we examine the diffraction in the fully localized limit, i.e., for $\gamma \to \infty$, shown in Figure 7a. This is also known as the bracket-averaged Taylor expansion (BAT) approximation [67], and is equivalent to perfectly localized trajectories not dissimilar to the trajectories obtained in surface hopping simulations. In this case, the damping of the molecular (interference) term is absent, and as expected, there is little deterioration of the diffraction signal even at large values of q. In contrast, for the standard values of γ_α (taken from Thompson et al. [76]), there is a significant degradation of the diffraction signal at large values of q which persists at all times, as can be seen in Figure 7b. Given that the default width parameters are fitted to ground state molecules, it is not far-fetched that the most appropriate values will deviate from the standard γ_α values. We therefore consider, in the third scenario shown in Figure 7c, the diffraction when the width factors have been halved, i.e., $\gamma_\alpha/2$. This

leads to an even more delocalized wavepacket and has a dramatic effect on the diffraction signal, with the signal becoming very weak for $q > 15$ Å^{-1} (intensity below the height of the lowest contour in Figure 7c). Again, considering that the standard values of γ_α constitute a conservative estimate of the width of the wavepacket, this emphasizes the strong effect of the damping due to the delocalization of wavepackets.

In addition to the effect of the width parameters discussed above, we also observe in Figure 7 that the dispersion plays an important role in degrading the signal over time, in particular for $t > 50$ fs, similarly to what was observed in the calculations for D_2 and ethylene. This 50 fs time-scale is consistent with Figure 6, which indicates that the dynamics is comparatively uniform at early times (the so-called 'ballistic' nature of this particular reaction [35]), but diverges at later times ($t > 50$ fs in Figure 6).

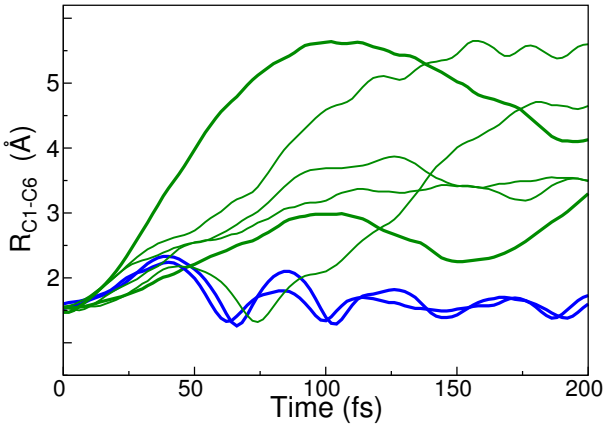

Figure 6. Representative C−C bondlength distances for the bond that breaks during the 1,3-cyclohexadiene (CHD) ring-opening reaction, shown as a function of time. Reproduced from Ref. [6]. Trajectories in blue lead back to the ring-closed form, while trajectories in green lead to the ring-open form of the molecule.

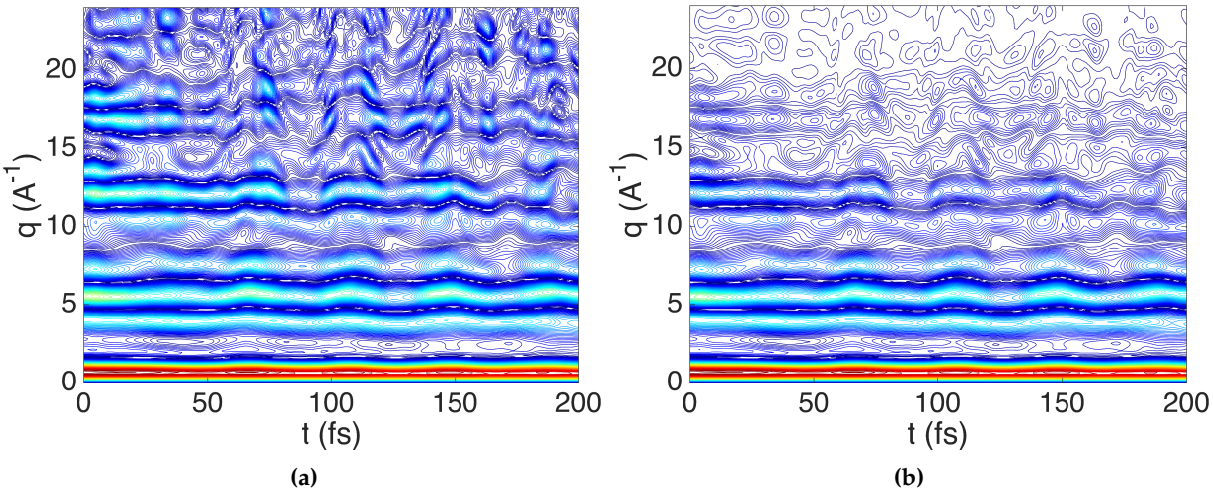

Figure 7. *Cont.*

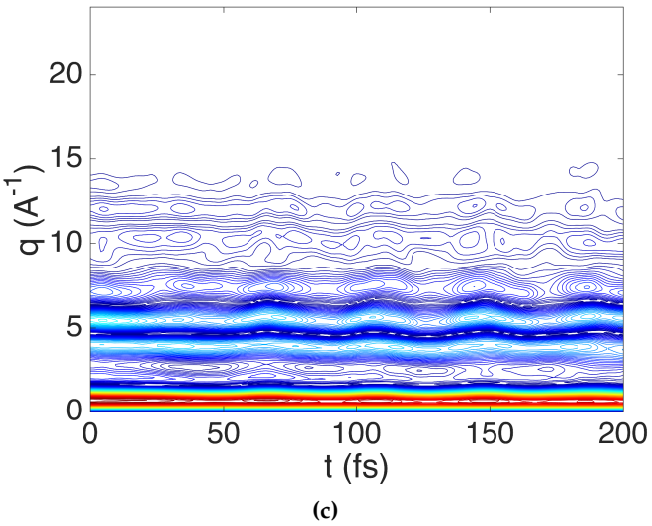

Figure 7. Contour plots of modified (elastic) scattering intensity, $M(q,t)$, for the ring-opening reaction of 1,3-cyclohexadiene (CHD) [6]. Time in fs and momentum transfer q in Å^{-1}, with $M(q,t)$ defined in Equation (16) (we use C-atom form factors in the denominator). (**a**) Perfectly localized trajectories with $\gamma_\alpha \to \infty$; (**b**) Standard values of the width parameters γ_α; (**c**) Increased width, i.e., more delocalized wavepackets, obtained via half-value $0.5\gamma_\alpha$ width parameters.

4. Discussion

Our analytical model in Section 3.1 indicates that degradation of the diffraction signal beyond q values of about 10–15 Å^{-1} is significant, with at least 50% of the signal lost by $q = 15$ Å^{-1}. This is a conservative estimate, since it is based on width factors fitted to ground state harmonic vibrational wavefunctions. These widths reflect the shape of the initially excited wavepacket in the Franck–Condon region above the ground state equilibrium geometry, which is why the Wigner distribution is used for sampling initial conditions in semi-classical propagation schemes [57]. However, subsequent propagation of the excited wavepacket leads to further dispersion. This is a general phenomenon, as emphasized by our simulations in three different molecules: D_2, 1,3-cyclohexadiene, and ethylene. In all three examples, the scattering signal degrades further with time as the wavepacket evolves.

In D_2 (Section 3.2.1), a diatomic molecule, we compare to a classically oscillating molecule and find that the diffraction signal is better defined and persists for all q when the nuclei are perfectly localized. Furthermore, we examine the effect of nuclear mass on the wavepacket, and find that the greater density of states associated with heavier atoms (or conversely a pump pulse with greater bandwidth) leads to greater initial localization. However, this sharper initial localization, which leads to better defined scattering, also leads to faster and more complete dispersion as the wavepacket evolves, degrading the scattering at longer times. In the ethylene molecule (Section 3.2.2), we examine the sensitivity of the scattering signal to the number of trajectories used in the simulations. We find that the number of trajectories correlates with the dispersion recorded in the scattering signal, such that a larger number of trajectories lead to an increased degradation of the signal. Strikingly, a small number of trajectories can qualitatively reproduce the scattering signal, indicating that a comparatively small number of trajectories can capture the essence of the reaction path and thus the diffraction signal, albeit while underestimating the dispersion at longer times. This finding is congruent with the analysis of recent ultrafast X-ray scattering experiments in 1,3-cyclohexadiene [6]. However, using not fully converged quantum molecular dynamics simulations, or equivalently just a small number of trajectories, introduces a sensitivity in the predicted diffraction patterns on the width parameters associated with each trajectory. In our simulations of 1,3-cyclohexadiene (Section 3.2.3), we examine this effect for the example of a larger, polyatomic molecule. Already with the standard and rather conservative width parameters, the scattering degrades notably at large values of q, and an additional

50% decrease in the width factors is sufficient to effectively quench the molecular diffraction signal for $q > 14$ Å^{-1}. This suggests that width parameters must be considered whenever ultrafast diffraction data for the time-evolution of molecular geometry is analysed.

Clearly, the concept of molecular geometry, in a classical sense, must be used with caution in the context of ultrafast processes and ultrafast diffraction in particular. The upside is that ultrafast diffraction experiments provide a sensitive probe of the delocalization of wavepackets, and one could consider using such experiments to determine, possibly time-dependent, width parameters that can be compared to quantum molecular simulations. Although molecular geometry is 'fuzzy' in time-evolving molecules, the wavepacket does have a distinct shape at all times. It is interesting to envision the use of ultrafast scattering to image the wavepacket in full detail, including for instance so-called quantum ripples [80]. This may only be possible in very small molecules, essentially diatomics, where direct inversion of the scattering signal is feasible. A similar resolution in a polyatomic molecule, although in principle possible, would certainly require advanced inversion algorithms and experiments that use alignment and/or tomographic techniques.

It is natural in this context to reflect on whether the dispersion of the wavepacket can be overcome via clever experimental setups. For instance, the shorter the duration of the pump pulse, the greater the initial localization, but this initial localization results in greater dispersion at later times. This is directly analogous to the calculations in D_2 and $\tilde{K}_2$ in this article, where the effect of an increased density of states for $\tilde{K}_2$ corresponds to the effect of shorter-duration, greater bandwidth pump pulses in an experiment. In practice, one often wishes to balance a degree of selectivity in the optical excitation against the achieved time resolution, since a pulse with very large bandwidth may simultaneously excite dynamics on several electronic states, leading to complex dynamics that are challenging to interpret [81]. Another possibility might be focusing. Most pump-probe experiments are performed with bandwidth-limited (i.e., transform-limited) pulses, which yield an initially localized wavepacket. As a consequence, the wavepacket naturally disperses and becomes more delocalized as it propagates for times $t > 0$. One could attempt to circumvent this by focusing the wavepacket at specific times using phase-shaped pump-pulses, enabling more accurate structure determinations at specific time points. However, first of all, such focusing would be unlikely to overcome the lower bound estimates of signal degradation at high q presented in our simple analytic model. Secondly, implementation of the focusing would add technical challenges to the already commanding experiments, essentially requiring a readjustment of the pulse shape for every time point on which to focus the wavepacket. While such an experiment might not necessarily help to elucidate reaction paths resulting from ordinary light exposure, it could add significant information about the potential energy surfaces involved and might help to optimize desired product yields.

5. Conclusions

The delocalization of nuclear wavepackets is a natural effect in molecular systems, and constitutes a fundamental property of wavepackets that cannot be easily circumvented. As the signal measured in scattering experiments is the transform of the molecular structure, the natural delocalization of structures during chemical reactions dampens the diffraction signal, particularly at large values of q, and implies a limit to the range of scattering vectors that yield useful information on the molecular dynamics. For the X-ray scattering experiments considered here, our simulations and analytical model suggest that there is little information beyond 10 to 15 Å^{-1}, at least for typical organic molecules. The sensitivity of scattering experiments to the shape of the wavepackets may offer an opportunity to experimentally measure them. Such measurements could be valuable for the development of advanced computational codes.

Ultrafast X-ray scattering experiments benefit from the exciting development of ultrashort pulsed free electron lasers. A challenge to date has been that the X-ray photon energy is limited, so that only rather small ranges of q can be probed. However, advances in accelerator technologies, in particular the build-out of LCLS-II at the SLAC National Accelerator Laboratory, promise harder X-rays and

a concommittant expanded q range. With a typical detector geometry covering scattering up to 60 degrees, 30 keV X-ray photons will reach up to $q = 15$ Å^{-1}. It therefore seems likely that the advances offered by LCLS-II will enable experimental determinations of wavepacket motions up to the useful maximum suggested by our simulations.

Acknowledgments: A.K. acknowledges funding from the Leverhulme Trust (RPG-2013-365), the European Union (FP7-PEOPLE-2013-CIG-NEWLIGHT), and the hospitality of Roland Lindh (Uppsala University) including sabbatical support from the Wenner–Gren Foundations. P.M.W. acknowledges support from the National Science Foundation, Grant No. CBET- 1336105, and by Defence Threat Reduction Agency, Grant Number HDTRA1-14-1-0008. This study benefitted from stimulating conversations with Jeremy Hastings and Michael Minitti from the SLAC National Accelerator Laboratory.

Author Contributions: A.K. and P.M.W. conceived and designed the calculations; A.K. performed the calculations; A.K. and P.M.W. analyzed the data; A.K. and P.M.W. wrote the article.

Conflicts of Interest: The authors declare no conflict of interest.

Abbreviations

The following abbreviations are used in this manuscript:

XFEL: X-ray Free-Electron Laser
LCLS: Linac Coherent Light Source
IAM: Independent Atom Model
CHD: 1,3-cyclohexadiene
FWHM: Full Width at Half Maximum

References

1. Mark, H.; Wierl, R. Über Elektronenbeugung am einzelnen Molekül. *Naturwissenschaften* **1930**, *18*, 205.
2. Hargittai, I.; Hargittai, M. *Stereochemical Applications of Gas-Phase Electron Diffraction: Part A the Electron Diffraction Technique*, 1st ed.; VCH: New York, NY, USA, 1988.
3. Warren, B.E. *X-ray Diffraction*; Courier Corporation: North Chelmsford, MA, USA, 1969.
4. Rentzepis, P.M.; Helliwell, J., Eds. *Time Resolved Electron and X-ray Diffraction*, 1st ed.; Oxford University Press: New York, NY, USA, 1997.
5. Ischenko, A.A.; Weber, P.M.; Miller, R.J.D. Capturing Chemistry in Action with Electrons: Realization of Atomically Resolved Reaction Dynamics. *Chem. Rev.* **2017**, submitted.
6. Minitti, M.P.; Budarz, J.M.; Kirrander, A.; Robinson, J.S.; Ratner, D.; Lane, T.J.; Zhu, D.; Glownia, J.M.; Kozina, M.; Lemke, H.T.; et al. Imaging molecular motion: Femtosecond X-ray scattering of an electrocyclic chemical reaction. *Phys. Rev. Lett.* **2015**, *114*, 255501.
7. Yang, J.; Guehr, M.; Shen, X.; Li, R.; Vecchione, T.; Coffee, R.; Corbett, J.; Fry, A.; Hartmann, N.; Hast, C.; et al. Diffractive Imaging of Coherent Nuclear Motion in Isolated Molecules. *Phys. Rev. Lett.* **2016**, *117*, 153002.
8. Glownia, J.M.; Natan, A.; Cryan, J.P.; Hartsock, R.; Kozina, M.; Minitti, M.P.; Nelson, S.; Robinson, J.; Sato, T.; van Driel, T.; et al. Self-Referenced Coherent Diffraction X-ray Movie of Ångström- and Femtosecond-Scale Atomic Motion. *Phys. Rev. Lett.* **2016**, *117*, 153003.
9. Stankus, B.; Budarz, J.M.; Kirrander, A.; Rogers, D.; Robinson, J.; Lane, T.J.; Ratner, D.; Hastings, J.; Minitti, M.P.; Weber, P.M. Femtosecond photodissociation dynamics of 1,4-diiodobenzene by gas-phase X-ray scattering and photoelectron spectroscopy. *Faraday Discuss.* **2016**, *194*, 525–536.
10. Budarz, J.M.; Minitti, M.P.; Cofer-Shabica, D.V.; Stankus, B.; Kirrander, A.; Hastings, J.B.; Weber, P.M. Observation of Femtosecond Molecular Dynamics via Pump-probe Gas Phase X-ray Scattering. *J. Phys. B* **2016**, *49*, 034001.
11. Minitti, M.P.; Budarz, J.M.; Kirrander, A.; Robinson, J.; Lane, T.J.; Ratner, D.; Saita, K.; Northey, T.; Stankus, B.; Cofer-Shabica, V.; et al. Toward structural femtosecond chemical dynamics: Imaging chemistry in space and time. *Faraday Discuss.* **2014**, *171*, 81–91.
12. Levantino, M.; Schiro, G.; Lemke, H.T.; Cottone, G.; Glownia, J.M.; Zhu, D.; Chollet, M.; Ihee, H.; Cupane, A.; Cammarata, M. Ultrafast myoglobin structural dynamics observed with an X-ray free-electron laser. *Nat. Commun.* **2015**, *6*, 6772.

13. Kim, K.H.; Kim, J.G.; Nozawa, S.; Sato, T.; Oang, K.Y.; Kim, T.W.; Ki, H.; Jo, J.; Park, S.; Song, C.; et al. Direct observation of bond formation in solution with femtosecond X-ray scattering. *Nature* **2015**, *518*, 385–389.
14. Bostedt, C.; Bozek, J.D.; Bucksbaum, P.H.; Coffee, R.N.; Hastings, J.B.; Huang, Z.; Lee, R.W.; Schorb, S.; Corlett, J.N.; Denes, P.; et al. Ultra-fast and ultra-intense X-ray sciences: First results from the Linac Coherent Light Source free-electron laser. *J. Phys. B* **2013**, *46*, 164003.
15. Pemberton, C.C.; Zhang, Y.; Saita, K.; Kirrander, A.; Weber, P.M. From the (1B) Spectroscopic State to the Photochemical Product of the Ultrafast Ring-Opening of 1,3-Cyclohexadiene: A Spectral Observation of the Complete Reaction Path. *J. Phys. Chem. A* **2015**, *119*, 8832–8845.
16. Fleming, G. *Chemical Applications of Ultrafast Spectroscopy*; Oxford University Press: New York, NY, USA, 1986.
17. Lorincz, A.; Novak, F.A.; Rice, S.A. Relaxation of Large Molecules Following Ultrafast Excitation. In *Ultrafast Phenomena IV*; Auston, D., Eisenthal, K., Eds.; Springer: Berlin/Heidelberg, Germany, 1984; Volume 38, pp. 387–389.
18. Andor, L.; Lörincz, A.; Siemion, J.; Smith, D.D.; Rice, S.A. Shot-noise-limited detection scheme for two-beam laser spectroscopies. *Rev. Sci. Instrum.* **1984**, *55*, 64–67.
19. Rosker, M.J.; Dantus, M.; Zewail, A.H. Femtosecond real-time probing of reactions. I. The technique. *J. Chem. Phys.* **1988**, *89*, 6113–6127.
20. Thompson, J.; Weber, P.M.; Estrup, P.J. Pump-Probe Low Energy Electron Diffraction. In Proceedings of the SPIE Conference on Time Resolved Electron and X-ray Diffraction, San Diego, CA, USA, 9 July 1995; Volume 2521, pp. 113–122.
21. Geiser, J.D.; Weber, P.M. Pump-probe diffraction imaging of vibrational wave functions. *J. Chem. Phys.* **1998**, *108*, 8004–8011.
22. Dudek, R.C.; Weber, P.M. Ultrafast Diffraction Imaging of the Electrocyclic Ring-Opening Reaction of 1,3-Cyclohexadiene. *J. Phys. Chem. A* **2001**, *105*, 4167–4171.
23. Gosselin, J.L.; Minitti, M.P.; Rudakov, F.M.; Solling, T.I.; Weber, P.M. Energy Flow and Fragmentation Dynamics of *N*,*N*-Dimethylisopropylamine. *J. Phys. Chem. A* **2006**, *110*, 4251–4255.
24. Cardoza, J.D.; Rudakov, F.M.; Weber, P.M. Electronic Spectroscopy and Ultrafast Energy Relaxation Pathways in the Lowest Rydberg States of Trimethylamine. *J Phys. Chem. A* **2008**, *112*, 10736–10743.
25. Kirrander, A.; Fielding, H.H. Coherent control in the continuum: Autoionisation of Xe. *J. Phys. B* **2007**, *40*, 897.
26. Suominen, H.J.; Kirrander, A. How to observe coherent electron dynamics directly. *Phys. Rev. Lett.* **2014**, *112*, 043002.
27. Bainbridge, A.R.; Harrington, J.; Kirrander, A.; Cacho, C.; Springate, E.; Bryan, W.A.; Minns, R.S. VUV Excitation of a Vibrational Wavepacket in D_2 Measured through Strong-Field Dissociative Ionization. *New J. Phys.* **2015**, *17*, 103013.
28. Kirrander, A.; Jungen, C.; Fielding, H.H. Control of ionization and dissociation with optical pulse trains. *Phys. Chem. Chem. Phys.* **2010**, *12*, 8948–8952.
29. Weber, P.M.; Thantu, N. Photoionization via transient states: A coherent probe of molecular eigenstates. *Chem. Phys. Lett.* **1992**, *197*, 556–561.
30. Thantu, N.; Weber, P.M. Dependence of two photon ionization photoelectron spectra on laser coherence bandwidth. *Chem. Phys. Lett.* **1993**, *214*, 276–280.
31. Thantu, N.; Weber, P.M. Resonant two photon ionization of phenanthrene via its transient S_2 state. *Z. Phys. D* **1993**, *28*, 191–194.
32. Freed, K.F.; Nitzan, A. Intramolecular vibrational energy redistribution and the time evolution of molecular fluorescence. *J. Chem. Phys.* **1980**, *73*, 4765–4778.
33. Lorincz, A.; Smith, D.D.; Novak, F.; Kosloff, R.; Tannor, D.J.; Rice, S.A. Rotational state dependence of pyrazine fluorescence: Initial decays for the vibrationless $^1B_{3u}$ state. *J. Chem. Phys.* **1985**, *82*, 1067–1072.
34. Novak, F.; Kosloff, R.; Tannor, D.J.; Lorincz, A.; Smith, D.D.; Rice, S.A. Wave packet evolution in isolated pyrazine molecules: Coherence triumphs over chaos. *J. Chem. Phys.* **1985**, *82*, 1073–1078.
35. Garavelli, M.; Page, C.S.; Celani, P.; Olivucci, M.; Schmid, W.E.; Trushin, S.A.; Fuss, W. Reaction Path of a sub-200 fs Photochemical Electrocyclic Reaction. *J. Phys. Chem. A* **2001**, *105*, 4458–4469.
36. Kirrander, A.; Fielding, H.H.; Jungen, C. Excitation, dynamics and control of rotationally autoionizing Rydberg states of H_2. *J. Chem. Phys.* **2007**, *127*, 164301.

37. Kirrander, A.; Jungen, C.; Fielding, H.H. Localization of electronic wave packets in H_2. *J. Phys. B* **2008**, *41*, 074022.
38. Kirrander, A.; Fielding, H.H.; Jungen, C. Optical phase and the ionization-dissociation dynamics of excited H_2. *J. Chem. Phys.* **2010**, *132*, 024313.
39. Shalashilin, D.V. Nonadiabatic dynamics with the help of multiconfigurational Ehrenfest method: Improved theory and fully quantum 24D simulation of pyrazine. *J. Chem. Phys.* **2010**, *132*, 244111.
40. Shalashilin, D.V. Multiconfigurational Ehrenfest approach to quantum coherent dynamics in large molecular systems. *Faraday Discuss.* **2011**, *153*, 105–116.
41. Levine, B.G.; Coe, J.D.; Virshup, A.M.; Martinez, T.J. Implementation of *ab initio* multiple spawning in the MOLPRO quantum chemistry package. *Chem. Phys.* **2008**, *347*, 3–16.
42. Makhov, D.V.; Glover, W.J.; Martinez, T.J.; Shalashilin, D.V. *Ab initio* multiple cloning algorithm for quantum nonadiabatic molecular dynamics. *J. Chem. Phys.* **2014**, *141*, 054110.
43. Richings, G.; Polyak, I.; Spinlove, K.; Worth, G.; Burghardt, I.; Lasorne, B. Quantum dynamics simulations using Gaussian wavepackets: The vMCG method. *Int. Rev. Phys. Chem.* **2015**, *34*, 269–308.
44. Shalashilin, D.V.; Child, M.S. The phase space CCS approach to quantum and semiclassical molecular dynamics for high-dimensional systems. *Chem. Phys.* **2004**, *304*, 103–120.
45. Shalashilin, D.V.; Child, M.S.; Kirrander, A. Mechanisms of double ionization in strong laser field from simulation with Coupled Coherent States. *Chem. Phys.* **2008**, *347*, 257–262.
46. Kirrander, A.; Shalashilin, D.V. Quantum dynamics with fermion coupled coherent states. *Phys. Rev. A* **2011**, *84*, 033406.
47. Heller, E.J. The semiclassical way to molecular spectroscopy. *Acc. Chem. Res.* **1981**, *14*, 368–375.
48. Makhov, D.V.; Saita, K.; Martinez, T.J.; Shalashilin, D.V. *Ab initio* multiple cloning simulations of pyrrole photodissociation: TKER spectra and velocity map imaging. *Phys. Chem. Chem. Phys.* **2015**, *17*, 3316–3325.
49. Saita, K.; Shalashilin, D.V. On-the-fly *ab initio* molecular dynamics with multiconfigurational Ehrenfest method. *J. Chem. Phys.* **2012**, *137*, 22A506.
50. Wolniewicz, L. Nonadiabatic energies of the ground state of the hydrogen molecule. *J. Chem. Phys.* **1995**, *103*, 1792–1799.
51. Staszewska, G.; Wolniewicz, L. Adiabatic Energies of Excited $^1\Sigma_u$ States of the Hydrogen Molecule. *J. Mol. Spectrosc.* **2002**, *212*, 208–212.
52. Wolniewicz, L.; Staszewska, G. $^1\Sigma_u^+ \rightarrow X^1\Sigma_g^+$ transition moments for the hydrogen molecule. *J. Mol. Spectrosc.* **2003**, *217*, 181–185.
53. Mohr, P.J.; Taylor, B.N.; Newell, D.B. CODATA Recommended Values of the Fundamental Physical Constants: 2010. *Rev. Mod. Phys.* **2012**, *84*, 1527.
54. Deb, S.; Weber, P.M. The Ultrafast Pathway of Photon-Induced Electrocyclic Ring-Opening Reactions: The Case of 1,3-Cyclohexadiene. *Ann. Rev. Phys. Chem.* **2011**, *62*, 19–39.
55. Makhov, D.V.; Martinez, T.J.; Shalashilin, D.V. Toward fully quantum modelling of ultrafast photodissociation imaging experiments. Treating tunnelling in the ab initio multiple cloning approach. *Faraday Discuss.* **2016**, *194*, 81–94.
56. Werner, H.J.; Knowles, P.J.; Knizia, G.; Manby, F.R.; Schütz, M.; others. *MOLPRO, Version 2012.1, a Package of Ab Initio Programs*.
57. Brown, R.C.; Heller, E.J. Classical trajectory approach to photodissociation: The Wigner method. *J. Chem. Phys.* **1981**, *75*, 186–188.
58. Tao, H.; Levine, B.G.; Martinez, T.J. *Ab Initio* Multiple Spawning Dynamics Using Multi-State Second-Order Perturbation Theory. *J. Phys. Chem. A* **2009**, *113*, 13656–13662.
59. Mori, T.; Glover, W.J.; Schuurman, M.S.; Martinez, T.J. Role of Rydberg States in the Photochemical Dynamics of Ethylene. *J. Phys. Chem. A* **2012**, *116*, 2808–2818.
60. Sellner, B.; Barbatti, M.; Müller, T.; Domcke, W.; Lischka, H. Ultrafast non-adiabatic dynamics of ethylene including Rydberg states. *Mol. Phys.* **2013**, *111*, 2439–2450.
61. Champenois, E.G.; Shivaram, N.H.; Wright, T.W.; Yang, C.S.; Belkacem, A.; Cryan, J.P. Involvement of a low-lying Rydberg state in the ultrafast relaxation dynamics of ethylene. *J. Chem. Phys.* **2016**, *144*, 014303.
62. Kobayashi, T.; Horio, T.; Suzuki, T. Ultrafast Deactivation of the $\pi\pi^*$(V) State of Ethylene Studied Using Sub-20 fs Time-Resolved Photoelectron Imaging. *J. Phys. Chem. A* **2015**, *119*, 9518–9523.

63. Tao, H. First Principles Molecular Dynamics and Control of Photochemical Reactions. Ph.D. Thesis, Stanford University, Stanford, CA, USA, 2011.
64. Eisenberger, P.; Platzman, P.M. Compton Scattering of X-rays from Bound Electrons. *Phys. Rev. A* **1970**, *2*, 415–423.
65. De Groot, F.; Kotani, A. *Core Level Spectroscopy of Solids*, 1st ed.; CRC Press: Boca Raton, FL, USA, 2008.
66. Henriksen, N.E.; Møller, K.B. On the Theory of Time-Resolved X-ray Diffraction. *J. Phys. Chem. B* **2008**, *112*, 558.
67. Kirrander, A.; Saita, K.; Shalashilin, D.V. Ultrafast X-ray Scattering from Molecules. *J. Chem. Theory Comput.* **2016**, *12*, 957–967.
68. Carrascosa, A.M.; Kirrander, A. *Ab initio* calculation of inelastic scattering. *Phys. Chem. Chem. Phys.* **2017**, doi:10.1039/C7CP02054F.
69. Møller, K.B.; Henriksen, N.E. Time-Resolved X-ray Diffraction: The Dynamics of the Chemical Bond. *Struct. Bond.* **2012**, *142*, 185.
70. Northey, T.; Zotev, N.; Kirrander, A. *Ab Initio* Calculation of Molecular Diffraction. *J. Chem. Theory Comput.* **2014**, *10*, 4911.
71. Northey, T.; Carrascosa, A.M.; Schäfer, S.; Kirrander, A. Elastic X-ray scattering from state-selected molecules. *J. Chem. Phys.* **2016**, *145*, 154304.
72. Carrascosa, A.M.; Northey, T.; Kirrander, A. Imaging rotations and vibrations in polyatomic molecules with X-ray scattering. *Phys. Chem. Chem. Phys.* **2017**, *19*, 7853–7863.
73. Prince, E. (Ed.) *International Tables for Crystallography Volume C: Mathematical, Physical and Chemical Tables*; Springer International Publishing: New York, NY, USA, 2006; ISBN 978-1-4020-1900-5.
74. Shorokhov, D.; Park, S.T.; Zewail, A.H. Ultrafast Electron Diffraction: Dynamical Structures on Complex Energy Landscapes. *ChemPhysChem* **2005**, *6*, 2228–2250.
75. Stefanou, M.; Saita, K.; Shalashilin, D.; Kirrander, A. Comparison of ultrafast X-ray and electron scattering—A computational study. *Chem. Phys. Lett.* **2017**, doi:10.1016/j.cplett.2017.03.007.
76. Thompson, A.L.; Punwong, C.; Martinez, T.J. Optimization of width parameters for quantum dynamics with frozen Gaussian basis sets. *Chem. Phys.* **2010**, *370*, 70–77.
77. Heller, E.J. Frozen Gaussians: A very simple semiclassical approximation. *J. Chem. Phys.* **1981**, *75*, 2923–2931.
78. Debye, P. Zerstreuung von Röntgenstrahlen. *Ann. Phys.* **1915**, *46*, 809–823.
79. Ben-Nun, M.; Martinez, T.J. Direct Observation of Disrotatory Ring-Opening in Photoexcited Cyclobutene Using ab Initio Molecular Dynamics. *J. Am. Chem. Soc.* **2000**, *122*, 6299–6300.
80. Katsuki, H.; Chiba, H.; Girard, B.; Meier, C.; Ohmori, K. Visualizing Picometric Quantum Ripples of Ultrafast Wave-Packet Interference. *Science* **2006**, *311*, 1589–1592.
81. Bellshaw, D.; Horke, D.A.; Smith, A.D.; Watts, H.M.; Jager, E.; Springate, E.; Alexander, O.; Cacho, C.; Chapman, R.T.; Kirrander, A.; et al. *Ab-initio* Surface Hopping and Multiphoton Ionisation Study of the Photodissociation Dynamics of CS_2. *Chem. Phys. Lett.* **2017**, doi:10.1016/j.cplett.2017.02.058.